scientific reports

Check for updates

OPEN

First-principles study of the electronic and optical properties of Ho_W impurities in single-layer tungsten disulfide

M. A. Khan[1] & Michael N. Leuenberger[2]✉

The electronic and optical properties of single-layer (SL) tungsten disulfide (WS_2) in the presence of substitutional Holmium impurities (Ho_W) are studied. Although Ho is much larger than W, density functional theory (DFT) including spin-orbit coupling is used to show that Ho:SL WS_2 is stable. The magnetic moment of the Ho impurity is found to be $4.75\mu_B$ using spin-dependent DFT. The optical selection rules identified in the optical spectrum match exactly the optical selection rules derived by means of group theory. The presence of neutral Ho_W impurities gives rise to localized impurity states (LIS) with f-orbital character in the band structure. Using the Kubo-Greenwood formula and Kohn-Sham orbitals we obtain atom-like sharp transitions in the in-plane and out-of-plane components of the susceptibility tensor, $\mathrm{Im}\chi_{\parallel}$ and $\mathrm{Im}\chi_{\perp}$. The optical resonances are in good agreement with experimental data.

Single-layer (SL) transition metal dichalcogenides (TMDs) are very attractive materials because of their special electronic and optical properties that enable lots of promising applications[1,2]. Since SL TMDs are semiconductors with a direct band gap[3,4], they can be used to build transistors and optoelectronic devices. Since the band gap is in the visible regime, photodetectors and solar cells can be developed. Growth processes typically introduce defects and impurities in SL TMDs with profound effects on their electronic, optical, and magnetic properties[5–7].

Over the past few years we have developed theoretical models based on density functional theory (DFT), tight-binding model, and 2D Dirac equation for the description of the electronic and optical properties of vacancy defects in TMDs[8–10], which are naturally occurring during different growth processes, such as mechanical exfoliation (ME), chemical vapor deposition (CVD), and physical vapor deposition (PVD). A central result of our papers is that group theory can be used to derive strict selection rules for the optical transitions, which are in excellent agreement with the susceptibility calculated by means of the Kubo-Greenwood formula using the Kohn–Sham orbitals.

In our recent paper in Ref.[10] we performed DFT calculations and obtained the optical spectrum of SL WS_2 in the presence of substitutional Er_W atoms. Although we did not include the effect of spin–orbit coupling (SOC), we obtained good agreement with Bai et al.'s experiments on Er-doped MoS_2 thin films using CVD growth[11] and wafer-scale layered Yb/Er co-doped WSe_2[12]. Similar results have been found by López-Morales et al.[13]. One of our motivations was to find out whether some of the LIS of Er lie within the band gap of SL WS_2. We were able to show that this is indeed the case. The reason for our motivation is that LIS inside the band gap of a semiconductor can be potentially used as a qubit or a qudit for quantum information processing. Remarkably, TMDs with rare-earth atoms (REAs) exhibit the unique property of strong isolation of their electrons in the unfilled 4f shell by the surrounding d shell. This property leads generally to high quantum yields, atom-like narrow bandwidths for optical transitions, long lifetimes, long decoherence times, high photostability, and large Stokes shifts. This strong isolation of the 4f electrons makes them behave like electrons in a free atom. Therefore, it is not surprising that Ce^{3+} impurities in yttrium aluminium garnet (YAG) can reach long coherence times of $T_2 = 2$ ms[14]. By replacing YAG with the calcium tungstate $CaWO_4$ as host material, it is possible to avoid the paramagnetic impurities of Y and substantially reduce the nuclear spin concentration without isotopic purification. Consequently, the Hahn echo experiment is able to achieve a long spin coherence time of $T_2 = 23$ ms for Er^{3+} impurities in $CaWO_4$[15].

[1]Department of Applied Physics, Federal Urdu University of Arts, Science and Technology, Islamabad, Pakistan. [2]NanoScience Technology Center, Department of Physics, and College of Optics and Photonics, University of Central Florida, Orlando, FL 32826, USA. ✉email: michael.leuenberger@ucf.edu

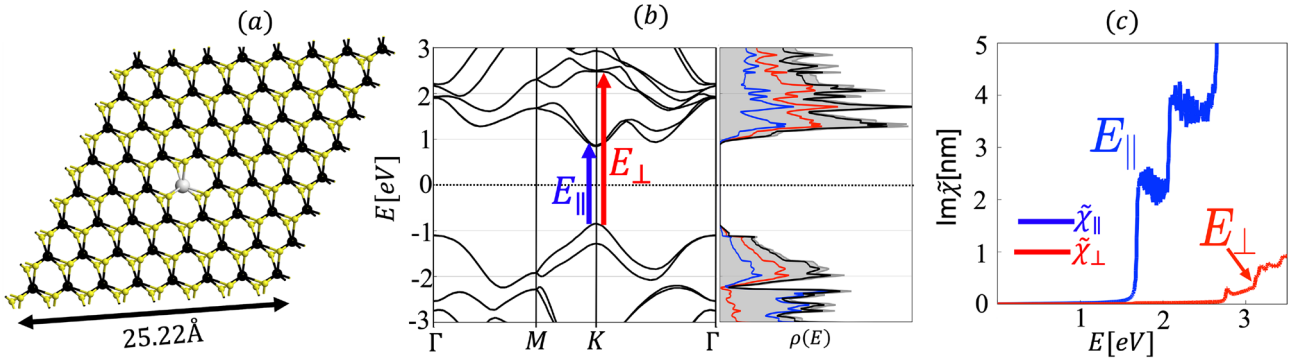

Figure 1. (**a**) Schematic shows a Ho_W impurity inside a $8 \times 8 \times 1$ supercell of SL WS_2. The grey circle depicts a Ho atom. The black (yellow) circles represent W (S) atoms. (**b**) The band structure and density of states (DOS) $\rho(E)$ of pristine SL WS_2 exhibits an in-plane band gap of $E_{\parallel} = 1.6$ eV and an out-of-plane band gap of $E_{\perp} = 3.2$ eV. States at the valence band edge are splitted due to SOC with $\Delta_{SOC} = 433$ meV. Gray region in the DOS plot specify the total DOS, while red blue and black curves are for *d*-orbitals of W, *p*-orbitals of S and the sum of the contributions, respectively. (**c**) Optical response of the pristine WS_2, showing the in-plane and out-of-plane band gaps.

Thus, it is advantageous to identify host materials for REAs with low concentrations or even free of paramagnetic impurities and nuclear spins. We argue here that TMDs are good candidates for such host materials.

Here, following Ref.[10], we calculate the electronic and optical properties of Ho_W impurities in SL WS_2. In particular, we find a peak at 2120 nm in the optical spectrum which is in good agreement with the characteristic wavelength of Ho observed in Ho:YAG lasers[16,17]. Laser systems that operate in the 2 μm range offer exceptional advantages for free space applications compared to conventional systems that operate at shorter wavelengths. This gives them a great market potential for the use in LIDAR and gas sensing systems and for direct optical communication applications. Besides, we find additional peaks in the optical spectrum of Ho_W:SL WS_2, which are a direct consequence of the D_{3h} symmetry of the Ho_W impurity and the interplay between the valley angular momentum (VAM), exciton angular momentum (EAM), and lattice angular momentum (LAM)[18].

The goal of this paper is to demonstrate the existence of localized Ho spin–orbit states inside the bandgap of WS_2, the ultra-narrow optical transitions due to the atom-like f-orbital states of Ho, and the strict optical selection rules by means of a combination of ab-initio DFT calculations, the Kubo-Greenwood formula, and group theory including SOC.

Bandstructure

Numerical analysis. All Numerical calculations are carried out by using DFT and with the use of Perdew–Burke–Ernzerhof (PBE) generalized gradient (GGA) parametrization[19] for exchange-correlation functional. Fully relativistic noncollinear and spin polarized DFT calculations were performed as implemented in the Synopsis Atomistix Toolkit (ATK) 2021.06[20]. For Ho_W impurity calculations, we consider a supercell consisting of eight unit cells along each crystalline-axis direction of the monolayer plane (i.e., 64 W atoms and 128 S atoms) and then replace a single W atom with Ho atom as shown in Fig. 1a). We consider a large supercell of edge length 25.22 Å, to fix the inter-impurity interactions. The point group of WS_2 with Ho_W defect is D_{3h}. The periodic structure of the superlattice allows one to characterize the electron states by the bandstructure $\varepsilon_n(\mathbf{k})$, where $\mathbf{k}$ is the vector in the first Brillouin zone of the superlattice and n enumerates different bands. The sampling of the Brillouin zone was done for a supercell with the equivalent of a 32×32×1 Monkhorst–Pack k-point grid for the WS_2 primitive unit cell with a cutoff energy of 400 Ry. For all calculations, structure is first geometrically optimized with a force tolerance of 0.05 eV/Å. The formation energy for the Ho_W impurity is calculated by means of the relation

$$E^f[\mathrm{Ho_W}] = E_{tot}[\mathrm{Ho_W}] - E_{tot}[\mathrm{host}] - \sum_i n_i \mu_i. \tag{1}$$

$E_{tot}[\mathrm{Ho_W}]$ and $E_{tot}[\mathrm{host}]$ are the total energy of the system with and without the impurity, respectively, n_i is the number of added ($n_i > 0$) or removed ($n_i < 0$) species of atoms during the formation of the impurity. μ_i's are chemical potentials of the W and Ho atoms, which are estimated from their corresponding bulk forms. The small value of the formation energy $E^f[\mathrm{Ho_W}] = 0.846$ eV, which corresponds to an energy increase of $E^f[\mathrm{Ho_W}]/64 = 13$ meV with respect to the unit cell of WS_2, indicates that the Ho_W impurity in $8 \times 8 \times 1$ WS_2 is thermodynamically stable. The thermodynamic stability can be shown by means of the cohesive energy per unit cell

$$E_{\mathrm{coh}} = E_{tot} - \sum_i n_i \mu_i. \tag{2}$$

C_{3h}		E	C_3	C_3^2	σ_h	S_3	S_3^5	linear	quadratic
A'	Γ_1	1	1	1	1	1	1	R_z	x^2+y^2, z^2
A''	Γ_4	1	1	1	−1	−1	−1	z	
E_1'	Γ_2	1	ξ	ξ^2	1	ξ	ξ^2	$x+iy$	(x^2-y^2, xy)
E_2'	Γ_3	1	ξ^2	ξ	1	ξ^2	ξ	$x-iy$	
E_1''	Γ_5	1	ξ	ξ^2	−1	$-\xi$	$-\xi^2$	R_x+iR_y	(xz, yz)
E_2''	Γ_6	1	ξ^2	ξ	−1	$-\xi^2$	$-\xi$	R_x-iR_y	
$^1E_{1/2}$	Γ_7	1	$-\xi^2$	$-\xi$	i	$i\xi^2$	$-i\xi$	$\left\vert\frac{1}{2},\frac{1}{2}\right\rangle, \left\vert\frac{3}{2},\frac{1}{2}\right\rangle$	
$^2E_{1/2}$	Γ_8	1	$-\xi$	$-\xi^2$	$-i$	$-i\xi$	$i\xi^2$	$\left\vert\frac{1}{2},-\frac{1}{2}\right\rangle, \left\vert\frac{3}{2},-\frac{1}{2}\right\rangle$	
$^1E_{3/2}$	Γ_{11}	1	−1	−1	i	i	$-i$	$\left\vert\frac{3}{2},\frac{3}{2}\right\rangle, \left\vert\frac{5}{2},\frac{3}{2}\right\rangle$	
$^2E_{3/2}$	Γ_{12}	1	−1	−1	$-i$	$-i$	i	$\left\vert\frac{3}{2},-\frac{3}{2}\right\rangle, \left\vert\frac{5}{2},-\frac{3}{2}\right\rangle$	
$^1E_{5/2}$	Γ_9	1	$-\xi$	$-\xi^2$	i	$i\xi$	$-i\xi^2$	$\left\vert\frac{5}{2},\frac{5}{2}\right\rangle$	
$^2E_{5/2}$	Γ_{10}	1	$-\xi^2$	$-\xi$	$-i$	$-i\xi^2$	$i\xi$	$\left\vert\frac{5}{2},-\frac{5}{2}\right\rangle$	

Table 1. Character table of the group C_{3h} with $\xi^3 = 1$. Two common notations are used for the IRs of the single and double group. The reduction of symmetry from D_{3h} to C_{3h} is accompanied by the compatibility relations $A_1', A_2' \to A', E' \to E_1' \bigoplus E_2'$, $A_1'', A_2'' \to A'', E'' \to E_1'' \bigoplus E_2''$, $E_{1/2} \to {}^1E_{1/2} \bigoplus {}^2E_{1/2}$, $E_{3/2} \to {}^1E_{3/2} \bigoplus {}^2E_{3/2}$, and $E_{5/2} \to {}^1E_{5/2} \bigoplus {}^2E_{5/2}$.

Using DFT, we obtain a cohesive energy for pristine WS_2 of −10.69553 eV and a cohesive energy for Ho:WS_2 with $8 \times 8 \times 1$ supercell of −677.10816 eV, which is equivalent to −10.579815 eV per unit cell of pristine WS_2. Both cohesive energies are negative and therefore both pristine WS_2 and Ho:WS_2 are thermodynamically stable. In agreement with the above argument using the formation energy, pristine WS_2 is a little more stable than Ho:WS_2. Therefore we can conclude that Ho:WS_2 at Ho doping concentrations of $\leq$ 1.56% is thermodynamically stable. This is consistent with the experimental evidence that Er:MoS_2 is stable at an Er doping concentration of 3%[11], and Er:$WeSe_2$ is stable at an Er/Yb co-doping concentration of 1.5% (1% Yb and 0.5% Er)[12].

Given the difference in atomic radii of Ho (1.75 Å) and W (2.1 Å), relaxing the Ho:SL WS_2 structure and comparing it with the bulk structure of SL WS_2 indicates that local strain is introduced by the Ho_W impurity in SL WS_2. This is evident from the slight bond length distortion near the Ho impurity. The atomic configuration of Ho doped SL WS_2 preserves the D_{3h} symmetry with 2.609 Å and 3.29 Å being the Ho–S and Ho–W bond lengths, respectively. In pristine WS_2 we find bond lengths of 2.42 Å and 3.18 Å for W–S and W–W bond lengths respectively. Thus, we obtain a local distortion of 8.75%.

We first obtain the results for bandstructure and electric susceptibility for pristine WS_2 as shown in Fig. 1b,c, values of the band gap (1.64 eV) and splitting of the valence band edge (425 meV) due to SOC, are in good agreement with previously reported values[21–24]. The crystal structure of SL WS_2 is three atoms thin, where W atom is sandwiched in between two S atoms (S–W–S) via strong covalent bonds. Pristine SL WS_2 is invariant with respect to σ_h reflection about the z = 0 (W) plane, where the z–axis is oriented perpendicular to the W plane of atoms. Therefore, electron states break down into two classes: even and odd, or symmetric and antisymmetric with respect to σ_h. d-Orbitals of the W and $p^{(t,b)}$-orbitals (t and b denoting the top and bottom layers) of the S atoms give the largest contribution to the conduction and valence band structure of SL WS_2[23,25]. Based on the σ_h symmetry, the even and odd atomic orbitals are spanned by the bases $\{\phi_1 = d^W_{x^2-y^2},\ \phi_2 = d^W_{xy},\ \phi_3 = d^W_{z^2},\ \phi_{4,5} = p^e_{x,y} = (p^{(t)}_{x,y}+p^{(b)}_{x,y})/\sqrt{2},\ \phi_6 = p^e_z = (p^{(t)}_z - p^{(b)}_z)/\sqrt{2}\}$ and $\{\phi_7 = d^W_{xz},\ \phi_8 = d^W_{yz},\ \phi_{9,10} = p^o_{x,y} = (p^{(t)}_{x,y} - p^{(b)}_{x,y})/\sqrt{2},\ \phi_{11} = p^o_z = (p^{(t)}_z + p^{(b)}_z)/\sqrt{2}\}$, respectively.

Using first principle studies[21–23], it is known that valence and conduction bands are primarily made from $d_{x^2-y^2}$, d_{xy} and d_{z^2} of W atoms, which transform as E_1', E_2' and A' irreducible representations (IRs) of the C_{3h} symmetry group at the K and K′ points, in the absence of SOC (Table 2). The presence of SOC couples the spin and orbital angular momenta, thereby requiring the consideration of the double-group IRs. Double-group IRs can be obtained by multiplying single-group IRs with $E_{1/2}$ as shown in Table 1, where $E_{1/2}$ is the 2D spin representation. The spin–orbit states for pristine SL WS_2 are shown in Fig. 6.

The isolated Ho atom has 11 4f electrons which are shielded by the outer $5s^25p^6$ electrons. In addition, Ho is trivalent in nature i.e. when placed in a crystal, Ho has the tendency of losing 3 electrons (1 from the 4f and 2 from the 5s orbitals). To confirm the trivalent nature of Ho, we perform a Mullikan population (MP) analysis and calculate the atomic charges in different orbitals of Ho in SL WS_2. The MP analysis shows that the 4f orbital of Ho is populated with an electron charge of 10.3e, whereas the 5s orbital is populated only with 0.372e, indicating a deficiency of 2.323e on Ho. Therefore to a sufficient approximation we consider the Ho impurity as Ho^{3+} ions in SL WS_2. The deficient electron charge of 2.323e on Ho is distributed in the entire supercell of Ho:SL WS_2. For example, the 6 neighboring S atoms share an extra electron charge of 0.84e, while the 6 next-nearest neighbor W atoms share an extra electron charge of 0.072e, when compared with the pristine case.

The bandstructure of WS_2 with Ho_W impurities is shown in Fig. 2. Regular electronic states within the valence or conduction bands are depicted by black lines while LIS (f-orbitals of Ho) are depicted by blue lines. Some of

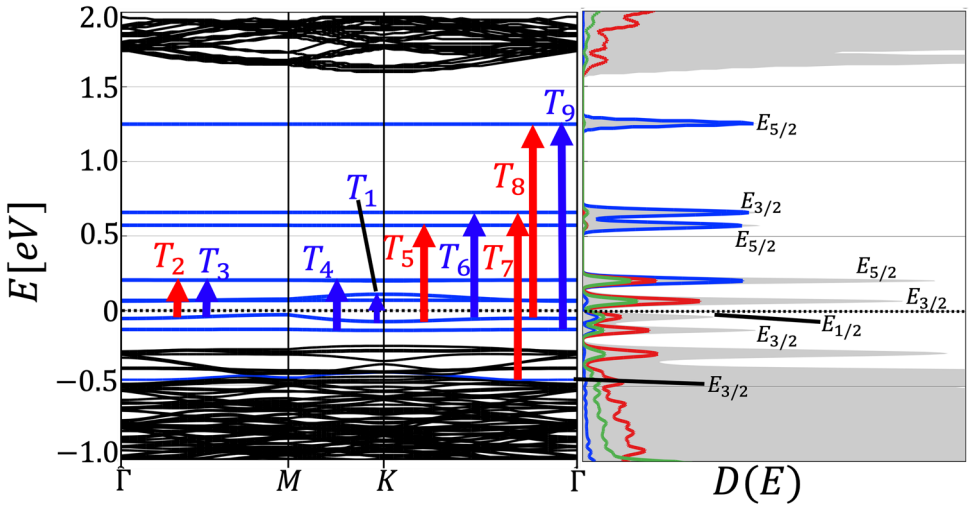

Figure 2. Bandstructure and density of states, shaded grey region shows the total density of states and the colored curves shows the projected density of states (Blue: f-orbitals of the Ho atom, Green: p-orbital of the neighboring S atoms and red: d-orbitals of the next neighbor W atoms) of $8 \times 8 \times 1$ supercell of WS_2 containing an Ho_W impurity. The LDS are clearly visible as dispersionless (localized) states, some of which lie inside the bandgap, others lie inside the valence band of WS_2. The eigenstates corresponding to the LIS transform according to the IRs of the point symmetry group D_{3h}. Vertical arrows indicate optical transitions corresponding to resonances shown in Fig. 7.

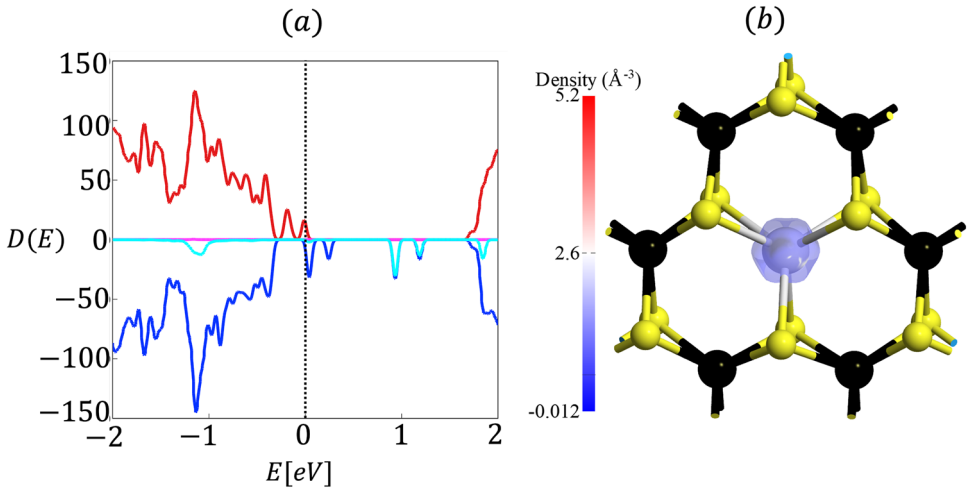

Figure 3. (**a**) Spin-polarized density of states for Ho_W:SL WS_2. Red (blue) is for spin-up (down) total Density of states while cyan (magenta) is for spin-up (down) projected density of states for Ho atom. (**b**) spin density $\rho_\uparrow - \rho_\downarrow$, concentrated on the Ho atom with a magnetic moment of $4.75\mu_B$. Spin density is plotted for an isovalue of 0.08911 $Å^{-3}$.

the allowed optical transitions between different f-orbitals of Ho are depicted by vertical arrows. The resulting optical spectrum is shown in Fig. 7.

The Kramers theorem states that for every energy eigenstate of a time-reversal symmetric system with half-integer total spin, there is at least one more eigenstate with the same energy. In other words, every energy level is at least doubly degenerate if it has half-integer spin. It can be seen that Kramers degeneracy, which is a consequence of time reversal symmetry, is broken for LIS in Ho_W:SL WS_2. In Ref.[26] it has been shown that presence of Ho_{Mo} impurity leads to spin polarization and results in long range ferromagnetic coupling between local spins. The local magnetic moment of the Ho_W impurity breaks the time reversal symmetry and lifts the Kramers degeneracy. In order to confirm that indeed the Ho_W impurity in SL WS_2 contains a magnetic moment, DFT calculations are performed by using spin-polarized GGA method. The results are presented in Fig. 3, where we show that the Ho impurity has a magnetic moment of $4.75\mu_B$. Our spin-polarized DFT calculations show that the exchange correlation potential leads to a spin splitting for Ho_W:SL WS_2. In Fig. 3b the isosurface plot for spin

D_{3h}		E	σ_h	$2C_3$	$2S_3$	$3C_2$	$3\sigma_v$	Linear	Quadratic
A_1'	Γ_1	1	1	1	1	1	1		x^2+y^2, z^2
A_2'	Γ_2	1	1	1	1	−1	−1	R_z	
A_1''	Γ_3	1	−1	1	−1	1	−1		
A_2''	Γ_4	1	−1	1	−1	−1	1	z	
E'	Γ_6	2	2	−1	−1	0	0	(x, y)	(x^2-y^2, xy)
E''	Γ_5	2	−2	−1	1	0	0	(R_x, R_y)	(xz, yz)
$E_{1/2}$	Γ_7	±2	0	±1	$\pm\sqrt{3}$	0	0	$\left\|\frac{1}{2},\pm\frac{1}{2}\right\rangle, \left\|\frac{3}{2},\pm\frac{1}{2}\right\rangle$	
$E_{3/2}$	Γ_9	±2	0	∓2	0	0	0	$\left\|\frac{3}{2},\pm\frac{3}{2}\right\rangle, \left\|\frac{5}{2},\pm\frac{3}{2}\right\rangle$	
$E_{5/2}$	Γ_8	±2	0	±1	$\mp\sqrt{3}$	0	0	$\left\|\frac{5}{2},\pm\frac{5}{2}\right\rangle$	

Table 2. Character table of the group D_{3h}. Two common notations are used for the IRs of the single and double group.

$\Gamma_i(D_{3h})$	A_1'	A_2'	A_1''	A_2''	E'	E''
$\Gamma_i \otimes E_{1/2}$	$E_{1/2}$	$E_{1/2}$	$E_{5/2}$	$E_{5/2}$	$E_{3/2} \oplus E_{5/2}$	$E_{1/2} \oplus E_{3/2}$

Table 3. Double-group IRs obtained from single-group IRs for D_{3h} group.

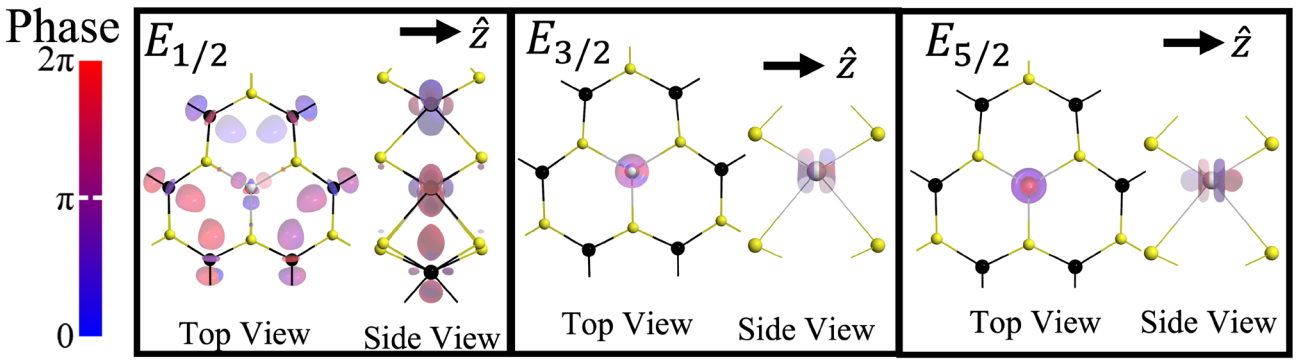

Figure 4. Examples of the Bloch states for the Ho_W impurity in $8 \times 8 \times 1$ super cell of WS_2.

density shows that the main contribution to the magnetism is due to the f-orbitals of Ho atom while the bulk states do not show any magnetic moment, in contrast to what has been observed in Ref.[26], where a long-range magnetic interaction is seen. The reason is that we consider a much larger supercell of $8 \times 8 \times 1$, as opposed to their $4 \times 4 \times 1$ supercell, resulting in a dilution of the impurity concentration that suppresses long-range magnetic interaction.

The Ho_W impurity preserves the σ_h symmetry and therefore can be described by the group D_{3h}[27,28], the irreducible representations (IRs) of which are shown in Table 2. The double-group IRs are obtained from the single-group IRs by taking the direct product with $E_{1/2}$, as shown in Table 3. Figure 4 shows three examples of LIS that appear in the band structure. The 3-fold rotation symmetry C_3 of the impurity is clearly visible.

Molecular orbital theory. A Ho_W impurity inside WS_2 looks similar to an atom in an effective electrostatic ligand field created by its neighboring six sulphur atoms. In this approximation molecular orbital theory (MOT) can be used. To identify the LIS in the DOS, the projected density of states (PDOS) showing orbital contributions of individual atoms is shown in Fig. 2. In addition to the contribution from the f orbitals of Ho_W, contributions from the p orbitals of the nearest neighboring S atoms and from the d orbitals of next-nearest neighboring W atoms are present. This means that in the Hilbert base spanned by $\psi_i^\dagger = (\phi_1, \ldots, \phi_{11}, \phi_{12} = f_{z^3}, \phi_{13} = f_{xz^2}, \phi_{14} = f_{yz^2}, \phi_{15} = f_{xyz}, \phi_{16} = f_{z(x^2-y^2)}, \phi_{17} = f_{x(x^2-3y^2)}, \phi_{18} = f_{y(3x^2-y^2)})^\dagger$, an LIS state can be represented by

$$\Psi = \sum_j a_j \phi_j, \tag{3}$$

where the real coefficients a_i's can be extracted from the PDOS shown in Fig. 2. Since admixture of orbitals is only allowed if they belong to the same IR, many coefficients are zero. The MOT diagram of pristine WS_2 can be found in Ref.[10]. The resulting eigenstates, identified by their IRs of D_{3h}, match the continuum states of the bands in WS_2, as can be seen from Ref.[29].

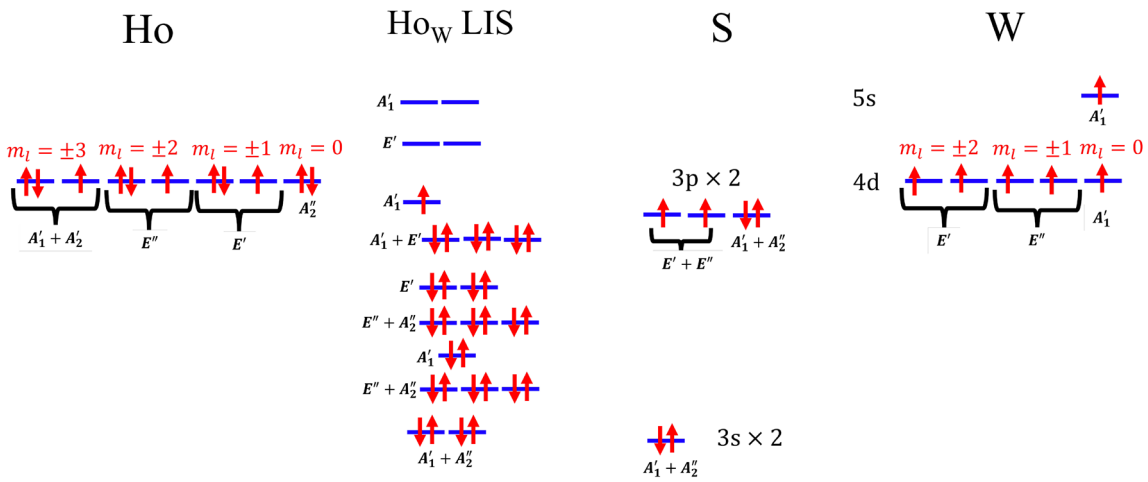

Figure 5. Molecular orbital diagram of Ho f orbitals in WS_2, giving rise to the Ho_W LIS shown in the bandstructure in Fig. 2. The states are labeled with the IRs of the point group D_{3h}.

Analyzing the PDOS, it becomes obvious that the Ho *f* orbitals couple to both the *p* orbitals of nearest neighboring S atoms and *d* orbitals of next-nearest neighboring W atoms. The resulting MOT diagram including Ho LIS is shown in Fig. 5. The orbital energy ordering can be determined by comparison with the PDOS shown in Fig. 2. The highest occupied molecular orbital (HOMO) is a $E_{1/2}$ spin-orbit state with an orbital A_1' singlet state. The lowest unoccupied molecular orbital (LUMO) is a $E_{3/2}$ spin-orbit state with a E' orbital doublet state, which matches the PDOS in Fig. 2. Although the Ho atom with an average atomic radius of 1.75 Å is substantially larger than a W atom with an average atomic radius of 1.35 Å, DFT shows that the Ho_W impurity is stable in the WS_2 host crystal. Because of the strong lattice distortions there are relatively strong hybridizations between the Ho *f* orbitals and the W *d* orbitals, as can be seen in the bandstructure in Fig. 2.

Optical response

Since the f-orbital contribution to the LIS is large, the optical spectrum exhibits narrow peaks, reminding of atom-like optical transitions. The relative dielectric functions ε_r of various TMDs have been measured in Ref.[30]. We evaluate the matrix elements of the dielectric tensor in three dimensions ($i, j = x, y, z$) using the Kubo–Greenwood formula for the electric susceptibility

$$\chi_{ij}(\omega) = \frac{e^2}{\hbar m_e^2 V} \sum_{uv\mathbf{k}} \frac{f_{u\mathbf{k}} - f_{v\mathbf{k}}}{\omega_{uv}^2(\mathbf{k})[\omega_{uv}(\mathbf{k}) - \omega - i\Gamma/\hbar]} p_{uv}^i p_{vu}^j \tag{4}$$

where $p_{pq}^j = \langle u\mathbf{k}|p^j|v\mathbf{k}\rangle$ is the dipole matrix element between Bloch states $\langle \mathbf{r}|u\,\mathbf{k}\rangle = \psi_{u\mathbf{k}}(\mathbf{r})$ and $\langle \mathbf{r}|v\,\mathbf{k}\rangle = \psi_{v\mathbf{k}}(\mathbf{r})$, V the volume of the crystal, f the Fermi function, and $\Gamma = 0.01$ eV the broadening. A vacuum separation of $a_3 = 20$ Å has been chosen in order to suppress not only electron bonding but also electrostatic interactions. In this limit the Bloch functions are localized on SL WS_2. Consequently, we can use the approximation $(1/V)\sum_{k_z} \to (1/\Omega a_3)$, where Ω is the surface area of SL WS_2. In this case $\tilde{\chi} = a_3\chi$, which has the unit of length, is independent of the vacuum separation. Using this definition, we present the in plane $\chi_\parallel$ and out of plane $\chi_\perp$ components of the 3D susceptibility tensor for Ho_W impurities in SL WS_2 in Fig. 7. We focus on transitions between states near the conduction and valence band edges and inside the band gap with resonance frequency $\hbar\omega_{uv} = |\varepsilon_u - \varepsilon_v|$, where ε_u is the eigenenergy of the Bloch state $\psi_{u\mathbf{k}}(\mathbf{r})$.

For pristine SL WS_2 the point group symmetry at the K and K' points is C_{3h} (see Table 1). A general result from group theory states that an optical transition is allowed by symmetry only if the direct product $\Gamma(|v\mathbf{k}\rangle)\otimes\Gamma(p^j)\otimes\Gamma(|u\mathbf{k}\rangle)$ contains $\Gamma(I)$ in its decomposition in terms of a direct sum. $\Gamma(I)$ denotes the IR for the identity, i.e., A' for C_{3h}. The in plane and out of plane components of p_{vu}^j must be considered individually because they transform according to different IRs of the point group. The resulting optical selection rules are shown in Fig. 6, which agree with the ones obtained from group theory shown in Table 4. These selection rules corroborate the difference between the in-plane and out-of-plane band gaps $E_{g||}$ and $E_{g\perp}$, respectively, which can be seen in the in-plane and out-of-plane susceptibilities $\mathrm{Im}[\chi_\parallel](\omega)$ and $\mathrm{Im}[\chi_\perp](\omega)$, respectively [see Fig. 1]. We predicted this difference in Refs.[8,9], which has later been experimentally confirmed[31,32]. This difference has also been verified theoretically by means of DFT calculations with GW correction and the solution of the Bethe-Salpeter equation for in-plane and out-of-plane excitons for similar crystals[33]. The band structure for pristine WS_2 in Fig. 1b shows in-plane and out-of-plane band gaps of $E_{g||} = 1.64$ eV and $E_{g\perp} = 3.12$ eV, respectively, which are in reasonable agreement with Refs.[34,35].

Alternatively, it is possible to use the conservation of angular momentum to derive the optical selection rules. In pristine SL WS_2 the C_3 rotational symmetry relaxes the atomic optical selection rules $\Delta m = \pm 1$ for $\sigma^\pm$ transitions and $\Delta m = 0$ for π transitions to $\Delta m = \pm 1 \pm 3$ for $\sigma^\pm$ transitions and $\Delta m = 0 \pm 3$ for π transitions, whereby an angular momentum mismatch of ± 3 can be transferred to or from the crystal lattice. The resulting optical selection rules match the ones obtained above from group theory and are also shown in Fig. 6. When

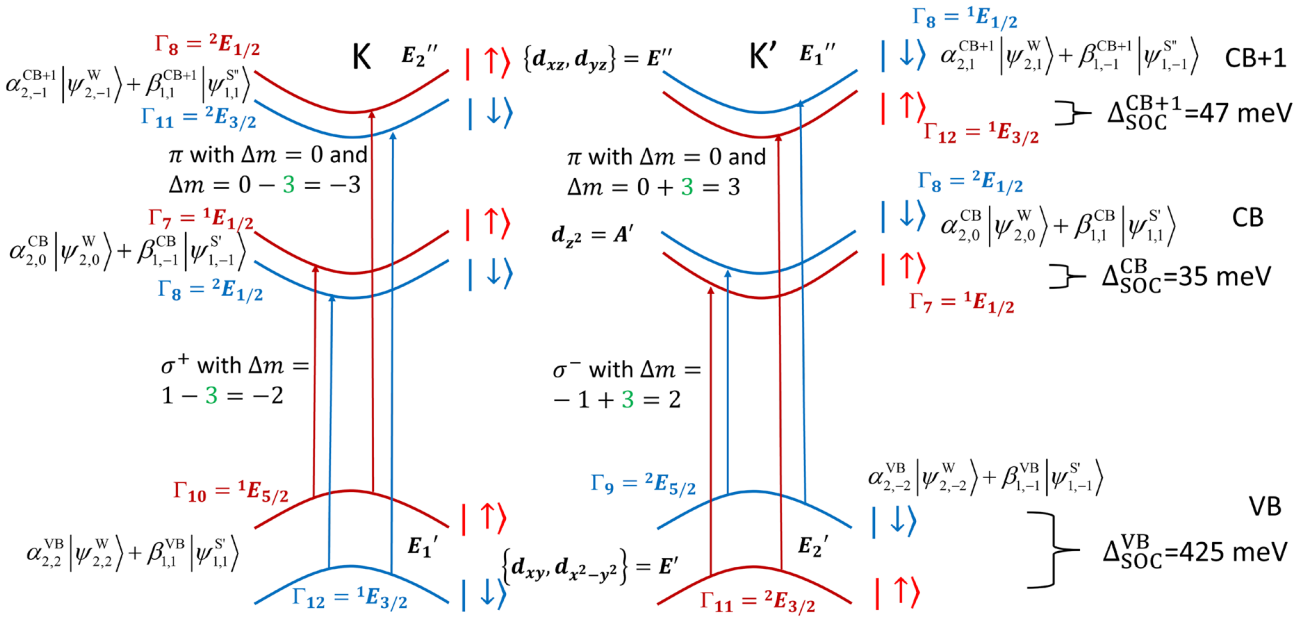

Figure 6. The optical selection rules in pristine SL WS_2 satisfy the equation $\Delta m = \pm 1 \pm 3$ for $\sigma^{\pm}$ transitions and $\Delta m = 0 \pm 3$ for π transitions. The term ± 3 is due to the C_3 rotational symmetry of the lattice. These selection rules corroborate the difference between the in-plane and out-of-plane band gaps $E_{g||}$ and $E_{g\perp}$, respectively. The Bloch states at the K and K' points transform according to the IRs of the C_{3h} point group. The coefficients of the main contributions are given by $|\alpha_{2,\pm 2}^{VB}|^2 = 0.75, |\beta_{1,\pm 1}^{VB}|^2 = 0.25, |\alpha_{2,0}^{CB}|^2 = 0.75$, $|\beta_{1,\pm 1}^{CB}|^2 = 0.19, |\alpha_{2,\pm 1}^{CB+1}|^2 = 0.56, |\beta_{1,\pm 1}^{CB+1}|^2 = 0.29$.

C_{3h}	A'	A''	E_1'	E_2'	E_1''	E_2''
A'		π	σ^-	σ^+		
A''	π				σ^-	σ^+
E_1'	σ^-		σ^+			π
E_2'	σ^+			σ^-	π	
E_1''		σ^-		π	σ^+	
E_2''		σ^+	π			σ^-

Table 4. Electric dipole selection rules in C_{3h} symmetry. σ represents in plane transitions while π represents out of plane transitions.

using the approximation of a two-band model described by a Dirac Hamiltonian for the conduction (CB) and valence (VB) bands, our selection rules match the ones shown in Ref.[18].

Given the point group symmetry of impurities in a crystal, the LIS transform according to its IRs. In the case of the Ho_W impurity the point group symmetry is D_{3h}, its character table shown in Table 2. The identity for D_{3h} is A_1'. Table 5 shows the the selection rules for electric dipole transitions for the IRs. Note that the electromagnetic field couples only to the orbital part of the Bloch states. Therefore the we need to consider only the orbital IRs of D_{3h}. Remarkably, we show in Table 6 that several optical transitions are in good agreement with available experimental data for optical transitions in Ho^{3+}:YAG.

Conclusion

Our results of electronic and optical properties of Ho_W impurities in SL WS_2 reveal LIS inside and near the band gap and atom-like sharp optical transitions both in $\chi_{\|}$ and $\chi_{\perp}$. Therefore, we argue that REAs in TMDs are good candidates for spin qubits. Let us elaborate further.

Atom-like sharp optical transitions suggest that the decoherence time should be very long, which is one of the main criteria for a spin qubit. As mentioned in the introduction, by choosing a host material free of paramagnetic impurities and nuclear spins, it would be possible to substantially increase the spin coherence time of the impurity spin, in this case the spin of a Ho_W impurity. Therefore, let us compare rare-earth atom spins in TMDs with other currently existing solid-state spin qubits:

- W has a weak abundance of 14% of nuclear spin (^{183}W) and S has a negligibly small abundance of 0.8% of nuclear spin 3/2 (^{33}S). These can be removed by isotopic purification. In stark contrast to that, electron spin

D_{3h}	A_1'	A_2'	A_1''	A_2''	E'	E''
A_1'				π	σ	
A_2'			π		σ	
A_1''		π				σ
A_2''	π					σ
E'	σ	σ			σ	π
E''			σ	σ	π	σ

Table 5. Electric Dipole selection rules in D_{3h} symmetry. σ represents in plane transitions while π represents out of plane transitions.

Ho^{3+} states	Ho^{3+}:YAG	Ho^{3+}:WS_2
$^5I_4 \rightarrow {}^5I_5$		5.1 μm (T_1)
$^5I_5 \rightarrow {}^5I_6$		3.75 μm (T_2) or 3.70 μm (T_3)
$^5I_6 \rightarrow {}^5I_7$		2.47 μm (T_4)
$^5I_7 \rightarrow {}^5I_8$	1.978 μm[17] 2.09 μm[16]	2.12 μm (T_5) or 1.78 μm (T_6)
$^5I_6 \rightarrow {}^5I_8$	1.169 μm[17]	1.19 μm (T_7) or 1.10 μm (T_8)
$^5I_5 \rightarrow {}^5I_8$	899 nm[17]	891 nm (T_9)

Table 6. Resonance wavelength of optical transitions (absorption and emission) for Ho^{3+}:YAG and Ho^{3+}:WS_2. The absorption transitions in Ho^{3+}:WS_2 are labeled according the optical spectrum shown in Fig. 7.

qubits in quantum dots made of GaAs suffer from hyperfine interaction. The issue is that Ga and As cannot be isotopically purified because all naturally abundant Ga and As isotopes have nuclear spins. Comparing to NV centers in diamond, N has a 99.6% abundance of nuclear spin 1 (^{14}N) and 0.4% of nuclear spin 1/2 (^{15}N). Therefore the nuclear spins of nitrogen cannot be removed by isotopic purification, either. In addition, P1 N impurities and surface spins are paramagnetic impurities that also lead to decoherence of an NV qubit. Consequently, we expect a much weaker decoherence of the Ho spin state.

- The location in the direction perpendicular to the plane of the 2D material of the rare-earth impurities is accurate on the atomic level. By contrast, in 3D materials, such as GaAs and diamond, impurities and defects are spread throughout the 3D materials. Therefore we expect enhanced quantum sensing due to accurate distance to target atoms.
- 2D materials have clean surfaces, in stark contrast to diamond that hosts dark P1 nitrogen impurities with nuclear spins and surface spins. The spin coherence time of shallow NV centers in diamond within 30 nm of the surface degrades drastically due to increased electric and magnetic noise. Diamond surfaces are difficult to be etched and polished in a controlled way due to diamond's hardness.[36]

Ce^{3+} in YAG exhibits electronic decoherence times of $T_2 = 2$ ms under dynamic decoupling[14]. This is relatively long considering that ^{27}Al, the only naturally occurring isotope, has a nuclear spin of 5/2. Liu et al. have recently performed the Deutsch-Jozsa quantum algorithm on the electron spin of a Ce^{3+} ion in YAG by means of phase gates with an operation time of $t_{op} = 0.3\,\mu s$[37]. This would allow for $N = T_2/t_{op} = 6.66 \times 10^3$ quantum operations. In the case of Er^{3+} impurities in $CaWO_4$, the spin coherence time is $T_2 = 23$ ms, without isotopic purification[15]. In principle, this would allow for $N = T_2/t_{op} = 6.66 \times 10^4$ quantum operations.

Since WS_2 can be isotopically purified to have zero nuclear spin, we expect even longer decoherence times and better performance with REAs in TMDs. In Ref.[38] a six-hour coherence time for optically addressable nuclear spins in Eu^{3+}:Y_2SiO_5 has been demonstrated experimentally. Based on this long coherence time a nuclear spin qubit in TMDs could allow for $N > 7.2 \times 10^{10}$ quantum operations.

These advantages suggest that REAs embedded in 2D materials made of TMDs might be vastly superior to GaAs spin qubits and NV centers in diamond and could pave the way to realizing scalable quantum networks, scalable quantum computing, and ultrasensitive remote quantum sensing.

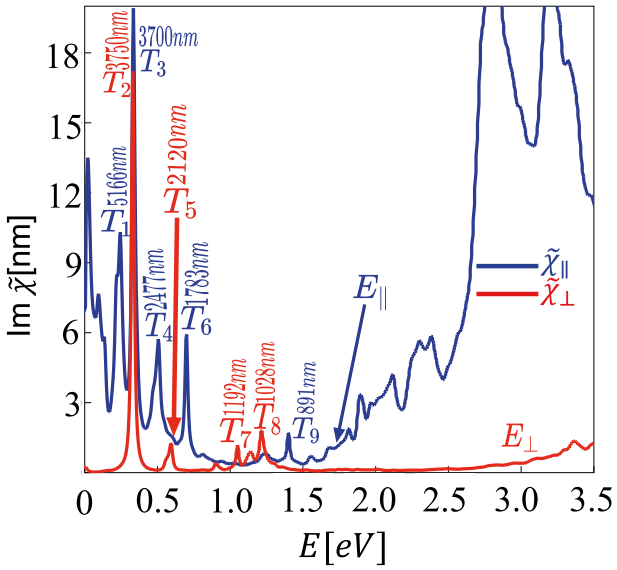

Figure 7. Optical spectrum calculated by means of ATK showing resonances of Im[$\varepsilon_{\|}$](ω) (blue) and Im[$\varepsilon_{\perp}$](ω) (red) *a*) due to Ho_W impurities in WS_2.

Data availability

The datasets used and/or analysed during the current study available from the corresponding author on reasonable request.

Received: 11 March 2022; Accepted: 8 June 2022
Published online: 06 July 2022

References

1. Wang, Q. H., Kalantar-Zadeh, K., Kis, A., Coleman, J. N. & Strano, M. S. Electronics and optoelectronics of two-dimensional transition metal dichalcogenides. *Nat. Nano* **7**, 699 (2012).
2. Mak, K. F. & Shan, J. A. U. Photonics and optoelectronics of 2D semiconductor transition metal dichalcogenides. *Nat. Photon* **10**, 216 (2016).
3. Mak, K. F., Lee, C., Hone, J., Shan, J. & Heinz, T. F. Atomically thin MoS_2: A new direct-gap semiconductor. *Phys. Rev. Lett.* **105**, 136805 (2010).
4. Splendiani, A. *et al.* Emerging photoluminescence in monolayer MoS2. *Nano Lett.* **10**, 1271 (2010).
5. Liu, D., Guo, Y., Fang, L. & Robertson, J. Sulfur vacancies in monolayer MoS2 and its electrical contacts. *Appl. Phys. Lett.* **103**, 183113 (2013).
6. Zhang, X. & Li, Q. Electronic and magnetic properties of nonmetal atoms adsorbed ReS2 monolayers. *J. Appl. Phys.* **118**, 064306 (2015).
7. Banhart, F., Kotakoski, J. & Krasheninnikov, A. V. Structural defects in graphene. *ACS Nano* **5**, 26 (2011).
8. Erementchouk, M., Khan, M. A. & Leuenberger, M. N. Optical signatures of states bound to vacancy defects in monolayer MoS_2. *Phys. Rev. B* **92**, 121401 (2015).
9. Khan, M. A., Erementchouk, M., Hendrickson, J. & Leuenberger, M. N. Electronic and optical properties of vacancy defects in single-layer transition metal dichalcogenides. *Phys. Rev. B* **95**, 245435 (2017).
10. Khan, M. A. & Leuenberger, M. N. Ab initio calculations for electronic and optical properties of ErW defects in single-layer tungsten disulfide. *J. Appl. Phys.* **130**, 115104 (2021).
11. Bai, G. *et al.* 2D layered materials of rare-earth Er-doped MoS2 with NIR-to-NIR down- and up-conversion photoluminescence. *Adv. Mater.* **28**, 7472 (2016).
12. Bai, G., Yang, Z., Lin, H., Jie, W. & Hao, J. Lanthanide Yb/Er co-doped semiconductor layered WSe2 nanosheets with near-infrared luminescence at telecommunication wavelengths. *Nanoscale* **10**, 9261 (2018).
13. G. I. López-Morales, A. Hampel, G. E. López, V. M. Menon, J. Flick, & C. A. Meriles, Ab-initio investigation of Er3+ defects in tungsten disulfide. *Comput. Mater. Sci.* 111041 (2021)
14. Siyushev, P. *et al.* Coherent properties of single rare-earth spin qubits. *Nat. Commun.* **5**, 3895 (2014).
15. Dantec, M. L. *et al.* Twenty-three–millisecond electron spin coherence of erbium ions in a natural-abundance crystal. *Sci. Adv.* **7**, 9786 (2021).
16. So, S. *et al.* Intra-cavity side-pumped Ho:YAG laser. *Opt. Express* **14**, 10481 (2006).
17. Malinowski, M., Frukacz, Z., Szuflińska, M., Wnuk, A. & Kaczkan, M. Optical transitions of Ho3+ in YAG. *J. Alloys Compounds* **300–301**, 389 (2000).
18. J. Xiao, Z. Ye, Y. Wang, H. Zhu, Y. Wang, & X. Zhang, Nonlinear optical selection rule based on valley-exciton locking in monolayer ws2. *Light Sci. Appl.* **4**, e366
19. Perdew, J. P. & Zunger, A. Self-interaction correction to density-functional approximations for many-electron systems. *Phys. Rev. B* **23**, 5048 (1981).
20. http://www.quantumwise.com/. (2019)
21. Xiao, D., Liu, G.-B., Feng, W., Xu, X. & Yao, W. Coupled spin and valley physics in monolayers of MoS_2 and other group-VI dichalcogenides. *Phys. Rev. Lett.* **108**, 196802 (2012).

22. Liu, G.-B., Shan, W.-Y., Yao, Y., Yao, W. & Xiao, D. Three-band tight-binding model for monolayers of group-VIB transition metal dichalcogenides. *Phys. Rev. B* **88**, 085433 (2013).
23. Zhu, Z. Y., Cheng, Y. C. & Schwingenschlögl, U. Giant spin-orbit-induced spin splitting in two-dimensional transition-metal dichalcogenide semiconductors. *Phys. Rev. B* **84**, 153402 (2011).
24. Zibouche, N., Kuc, A., Musfeldt, J. & Heine, T. Transition-metal dichalcogenides for spintronic applications. *Annalen der Physik* **526**, 395 (2014).
25. Cappelluti, E., Roldán, R., Silva-Guillén, J. A., Ordejón, P. & Guinea, F. Tight-binding model and direct-gap/indirect-gap transition in single-layer and multilayer MoS_2. *Phys. Rev. B* **88**, 075409 (2013).
26. Zhao, Q., Zhai, C., Lu, Q. & Zhang, M. Effect of Ho dopant on the ferromagnetic characteristics of MoS2 nanocrystals. *Phys. Chem. Chem. Phys.* **21**, 232 (2019).
27. Cheiwchanchamnangij, T., Lambrecht, W. R. L., Song, Y. & Dery, H. Strain effects on the spin-orbit-induced band structure splittings in monolayer MoS_2 and graphene. *Phys. Rev. B* **88**, 155404 (2013).
28. Song, Y. & Dery, H. Transport theory of monolayer transition-metal dichalcogenides through symmetry. *Phys. Rev. Lett.* **111**, 026601 (2013).
29. Pike, N. A. *et al.* Origin of the counterintuitive dynamic charge in the transition metal dichalcogenides. *Phys. Rev. B* **95**, 201106 (2017).
30. Li, Y. *et al.* Measurement of the optical dielectric function of monolayer transition-metal dichalcogenides: MoS_2, $MoSe_2$, WS_2, and WSe_2. *Phys. Rev. B* **90**, 205422 (2014).
31. Wang, G. *et al.* In-plane propagation of light in transition metal dichalcogenide monolayers: optical selection rules. *Phys. Rev. Lett.* **119**, 047401 (2017).
32. Xu, Z. *et al.* Optical detection of the susceptibility tensor in two-dimensional crystals. *Commun. Phys.* **4**, 215 (2021).
33. Guilhon, I. *et al.* Out-of-plane excitons in two-dimensional crystals. *Phys. Rev. B* **99**, 161201 (2019).
34. Hsu, C. *et al.* Thickness-dependent refractive index of 1L, 2L, and 3L MoS2, MoSe2, WS2, and WSe2. *Adv. Opt. Mater.* **7**, 1900239 (2019).
35. Sauer, M. O., Nielsen, C. E. M., Merring-Mikkelsen, L. & Pedersen, T. G. Optical emission from light-like and particle-like excitons in monolayer transition metal dichalcogenides. *Phys. Rev. B* **103**, 205404 (2021).
36. de Leon, N. P. *et al.* Materials challenges and opportunities for quantum computing hardware. *Science* **372**, eabb2823 (2021).
37. Liu, Z. *et al.* Electric field manipulation enhanced by strong spin-orbit coupling: Promoting rare-earth ions as qubits. *Natl. Sci. Rev.* **7**, 1557 (2020).
38. Zhong, M. *et al.* Optically addressable nuclear spins in a solid with a six-hour coherence time. *Nature* **517**, 177 (2015).

Acknowledgements

We acknowledge support provided by DARPA under Grant no. HR00112220011.

Author contributions

All authors contributed equally to this manuscript.

Additional information

Correspondence and requests for materials should be addressed to M.N.L.

Reprints and permissions information is available at www.nature.com/reprints.

Publisher's note Springer Nature remains neutral with regard to jurisdictional claims in published maps and institutional affiliations.